



Wind wave and water level dataset for Hornsund, Svalbard (2013–2021)

Zuzanna M. Swirad¹, Mateusz Moskalik¹, and Agnieszka Herman²

¹Institute of Geophysics, Polish Academy of Sciences, Warsaw, Poland

²Institute of Oceanology, Polish Academy of Sciences, Sopot, Poland

Correspondence: Zuzanna M. Swirad (zswirad@igf.edu.pl)

Received: 13 January 2023 – Discussion started: 25 January 2023

Revised: 23 May 2023 – Accepted: 1 June 2023 – Published: 27 June 2023

Abstract. Underwater pressure sensors were deployed near-continuously at various locations of the nearshore (8–23 m depth) Hornsund fjord, Svalbard, between July 2013 and February 2021. Raw pressure measurements at 1 Hz were used to derive mean water levels, wave spectra and bulk wave parameters for 1024 s bursts at hourly intervals. The procedure included subtracting atmospheric pressure, depth calculation, fast Fourier transform, correction for the decrease of the wave orbital motion with depth and adding a high-frequency tail. The dataset adds to the sparse in situ measurements of wind waves and water levels in the Arctic, and it can be used, for example, for analysing seasonal wind wave conditions and inter-annual trends and calibrating/validating wave models. The dataset is stored in the PANGAEA repository (<https://doi.org/10.1594/PANGAEA.954020>; Swirad et al., 2023).

1 Introduction

In situ wave measurements are critical for understanding wave climate, analysing seasonal and inter-annual trends, and calibrating and validating wave transformation models (e.g. Reistad et al., 2011). The spatial distribution of instruments providing wind wave data is irregular and tends to concentrate in mid- and low-latitude coastal areas (e.g. <https://www.ndbc.noaa.gov/>, 28 November 2022; Semedo et al., 2015). In the Arctic, the network of such instruments is particularly sparse. There is a pertinent lack of continuous wave data in the Svalbard archipelago where communities, industry infrastructure, and research stations are located. Continuous wave observations in the coastal Arctic are needed to better understand how the following contribute to coastal flooding and erosion that can cause infrastructure damage (Forbes, 2011): (i) decreasing sea-ice extent – pan-Arctic annual mean extent decrease of 3.5%–4.1% per decade (IPCC, 2019) or 1.5- to 3-fold increase in the length of the sea-ice-free season along pan-Arctic coasts (Barnhart et al., 2014) between 1979 and 2012; (ii) increasing frequency and strength of storms (Francis et al., 2011; Wang et al., 2015; Stopa et al.,

2016; Waseda et al., 2018); and, in consequence, (iii) higher waves acting on Arctic coasts for longer time periods.

Our knowledge of the western Svalbard wave climate comes primarily from global spectral models such as NOAA's WaveWatch III (WW3) hindcast (WW3DG, 2019); ECMWF reanalysis projects ERA-40 (1957–2002; Uppala et al., 2005), ERA-Interim (1979–2019; Dee et al., 2011), and ERA5 (1959–present; Hersbach et al., 2020); or NCEP's Climate Forecast System Reanalysis (CFSR; Saha et al., 2014). Arctic Ocean Wave Analysis and Forecast system (Carrasco et al., 2022) is a shorter-duration (since 2017), higher-resolution (3 km) model that provides hourly significant wave height (H_s), peak period (T_p) and peak wave direction (θ_p) using ECMWF's Ocean Wave Model (WAM). The 10 km resolution ERA-40 reanalysis data allowed Semedo et al. (2015) to capture seasonal trends in swell and wind sea and the ≥ 10 cm per decade increase in winter H_s over the northern Atlantic. Stopa et al. (2016) used CFSR and altimetry data to calculate an average H_s of 1.5 m (99th percentile of 5–6 m) for the period 1992–2014 west of Svalbard. Wojtysiak et al. (2018) observed up to 1 m H_s difference between winter (higher) and summer (lower) months using WW3

(2005–2015; at 0.5° resolution) and ERA-Interim (1979–2015; at 1° resolution), and they found a statistically significant trend of increasing frequency (2 storms per decade) and total duration (4 d per decade) of storms for the Greenland Sea off south-western Svalbard for the 1979–2015 period, with the typical annual values of 10–40 storms and 20–80 d, respectively.

The large-scale models are good for understanding the general trends in the Arctic/Svalbard area but provide limited information on local-scale wave parameters in specific fjords and bays (Nederhoff et al., 2022). How the open ocean wave conditions translate into wave conditions in the coastal areas is poorly constrained given complex coastal wind patterns and bottom topography (Semedo et al., 2015). Moreover, the large-scale models oversimplify most aspects of wind wave–sea ice interactions. Most operational models use simple empirical formulae for wave attenuation in sea ice (Barnhart et al., 2014; Zhao et al., 2015; Ardhuin et al., 2016).

Herman et al. (2019) used three nested Simulating WAVes Nearshore (SWAN; Booij et al., 1999) models to predict wind wave parameters within bays of Hornsund fjord (~ 15 m depth), taking eastern Greenland Sea WW3 spectra as boundary conditions. They ran the model for two sea-ice-free 4-month periods (August–November 2015 and 2016), finding a good agreement between the modelled and measured significant wave height ($r^2 > 0.9$) and mean absolute wave period ($r^2 = 0.63$ – 0.78). The study added considerable detail to wind wave transformation in the nearshore environment of Hornsund by including fjord bathymetry, which allowed for resolving depth-induced wave breaking and bottom friction on wind conditions. Notably, the study used a subset of the dataset described in this paper to validate the wave spectral model (Herman et al., 2019).

The model of Herman et al. (2019) tested against buoy data performed well for ice-free conditions only. For a bay of the Beaufort Sea, Nederhoff et al. (2022) incorporated sea ice into the SWAN model, which enabled them to reliably describe wave climate in 1979–2019. The need for observational data to validate wave models, especially in periods when the sea ice is present, persists.

We present a 7.5-year (July 2013 to February 2021) wind wave dataset from Hornsund, southern Svalbard (77° N, 15.5° E). Our goal is to increase observational understanding of Arctic wave conditions by providing a dataset that can be further used to (i) analyse the inter- and intra-annual trends in nearshore wind wave conditions, (ii) calibrate and validate wave transformation models, (iii) quantify the role of sea ice in wave attenuation, (iv) create empirical models of wave run-up on high-latitude beaches, and (v) predict future wind wave conditions.

2 Study area

Hornsund is an ~ 30 km long fjord of SW Spitsbergen, Svalbard (Fig. 1a). It has an ~ 12 km wide and ~ 100 m deep opening to the Greenland Sea. The average fjord depth is ~ 100 m with the deeper (200–250 m) central part (Fig. 1b; Herman et al., 2019). The tides are semi-diurnal, and the average tidal range is 0.75 m (Kowalik et al., 2015). The circulation is cyclonic (anticlockwise) with the inflow from SW and outflow to the NW (Jakacki et al., 2017).

In 1979–2018 easterly winds dominated at the Polish Polar Station (12 m a.s.l.; PPS in Fig. 1e) with the mean direction of 124° (annual mean range of 102 – 140°). Mean wind speed at ~ 20 m a.s.l. was 5.5 m s^{-1} (Wawrzyniak and Osuch, 2020).

Wave conditions in Hornsund are usually related to the long oceanic swell or mixed swell/wind sea from S–SW with short wind waves formed locally due to predominantly easterly winds. The mean H_s at the fjord mouth is 1.2–1.3 m, decreasing to 0.5–0.9 m in the central and to < 0.4 m in the inner parts of Hornsund (Fig. 1c). Northern shores of the fjord receive more wave energy than southern shores (Herman et al., 2019).

Hornsund bays (in this study Hansbukta, Isbjørnhamna, Rettkvalbogen, Veslebogen and Gåshamna) have complex shapes and bottom topography with ubiquitous skerries causing strong wave transformation due to refraction and dissipation (Herman et al., 2019).

Sea ice forms locally in the fjord or drifts from the open Greenland Sea. The latter originates east of Svalbard, drifts past the southern tip of Spitsbergen (Sørkapp) and then drifts northwards along the western Spitsbergen coast with cold Sørkapp Current (blue arrow in Fig. 1a). Fast ice (i.e. sea ice attached to the shore) persists during winter months. Muckenhuber et al. (2016) observed a decrease in sea-ice (both drift and fast ice) duration and extent between 2000 and 2014. In summer months glacier ice from calving tide-water glaciers (Błaszczuk et al., 2019) may accumulate in bays. Increased storminess coincident with positive air temperature anomalies and the lack of sea ice, in particular during October–December, may contribute to coastal erosion (Zagórski et al., 2015).

3 Methods

3.1 Input data

Pressure data were collected between 21 July 2013 and 12 February 2021 using RBR virtuoso P (continuous sampling at 4 or 6 Hz interval), RBR duo TD (continuous sampling at 1 Hz interval) and RBR virtuoso wave sensors (1024 s bursts at 30 min interval with 1 Hz sampling interval or at 60 min interval with 2 Hz sampling interval). There were 24 single deployments with a duration of 13–599 d (Table 1; Fig. 2). Initially the deployments were short (< 100 d)

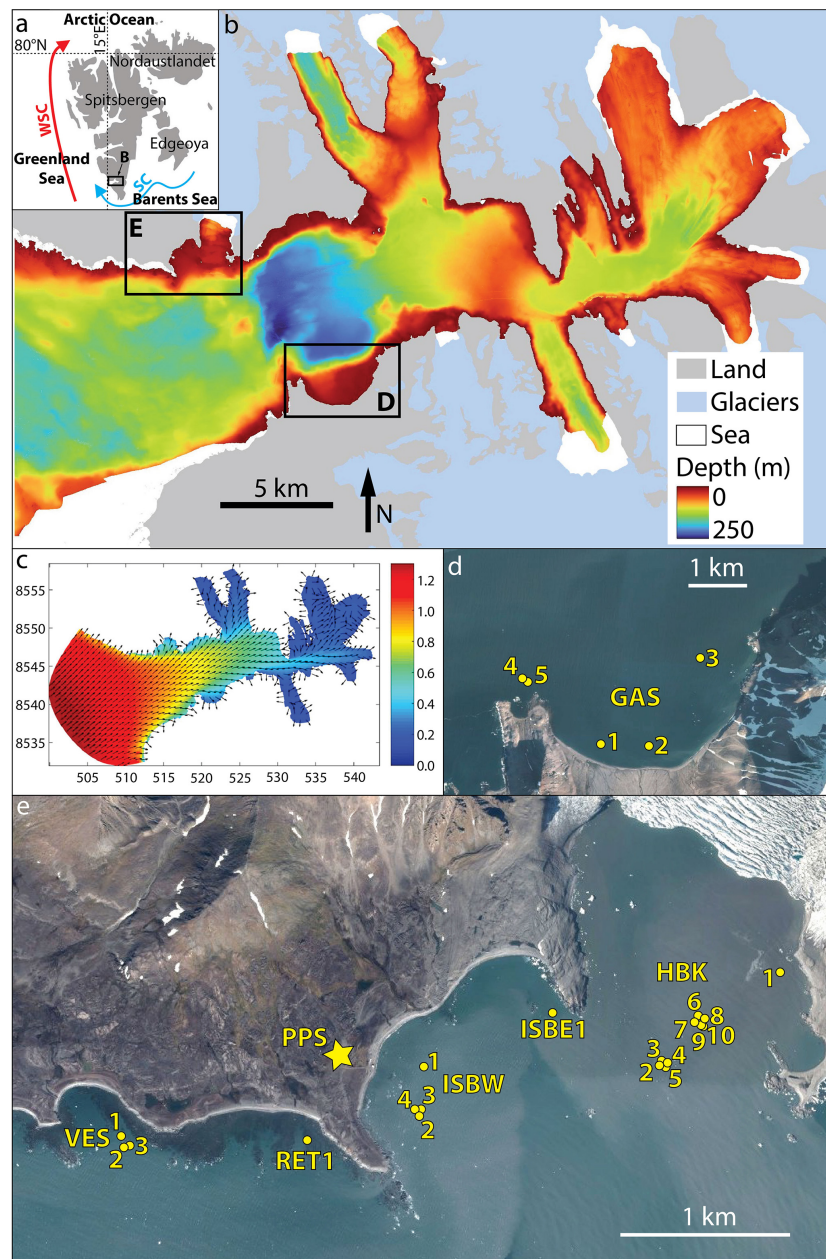


Figure 1. Study area: (a) Svalbard archipelago; WSC = warm West Spitsbergen Current; SC = cold Sørkapp Current; (b) bathymetry of Hornsund fjord (source: Norwegian Hydrographic Service; permit granted to IG PAS); (c) mean significant wave height, H_s (colours, in metres, m) and wind wave direction, θ_p (arrows) from Herman et al. (2019); axis labels refer to Universal Transverse Mercator coordinate system zone 33X (UTM33X) coordinates (in kilometres, km); location of sensor deployments in southern (d) and northern (e) Hornsund. HBK = Hansbukta, ISB = Isbjørnhamna (W = western, E = eastern), RET = Rettkvalbogen, GAS = Gåshamna, VES = Veslebogen, PPS = Polish Polar Station. Background image © Norwegian Polar Institute (permit granted).

and usually restricted to the fieldwork season (late spring to autumn). Since 2015, however, deployments were typically ~ 1 -year long with instrument recovery and redeployment during summer field campaigns. As a result of the COVID-19 pandemic, it was impossible to recover instruments in summer 2020, and the last two deployments (GAS5 and VES3) were > 550 d long and ended with the battery going dead.

The instruments were anchored to the seabed in various locations in northern (Hansbukta, western and eastern Isbjørnhamna, Rettkvalbogen, Veslebogen) and southern (Gåshamna) Hornsund (Fig. 1d and e). The raw pressure data are part of the LONGHORN oceanographic monitoring of the Institute of Geophysics, Polish Academy of Sciences, (IG PAS) and are provided in Swirad et al. (2022).

Table 1. Details of the pressure sensor deployments for in situ wave measurements in Hornsund, Svalbard. Deployment ID (DepID) refers to bays: HBK = Hansbukta, ISB = Isbjørnhamna (W = western, E = eastern), RET = Rettkvalbogen, GAS = Gåshamna, VES = Veslebogen. LONGHORN ID refers to the IG PAS oceanographic monitoring (Swirad et al., 2022).

DepID	LONGHORN ID	Start	End	Length (days)	Latitude (° N)	Longitude (° E)	Depth (m)	Instrument, serial number
HBK1	P01	21 Jul 2013	10 Aug 2013	21	77.0068	15.6509	8	RBR virtuoso P, 52915
HBK2	P02	5 Sep 2013	7 Dec 2013	94	77.0010	15.6243	23	RBR virtuoso P, 52915
HBK3	P03	1 Feb 2014	5 May 2014	94	77.0010	15.6243	23	RBR virtuoso P, 52916
HBK4	P04	1 Jun 2014	2 Sep 2014	94	77.0009	15.6245	23	RBR virtuoso P, 52915
HBK5	P05	25 Aug 2014	26 11 2014	94	77.0009	15.6245	23	RBR virtuoso P, 52916
HBK6	Wave01	10 Jun 2015	2 Jun 2016	359	77.0031	15.6298	22	RBR virtuoso wave, 52980
HBK7	Wave04	1 Jul 2016	21 May 2017	325	77.0031	15.6293	22	RBR virtuoso wave, 52980
HBK8	Wave08	9 Jun 2017	24 May 2018	350	77.0030	15.6316	22	RBR virtuoso wave, 55113
HBK9	TD01	5 Jun 2018	15 Jan 2019	225	77.0029	15.6311	22	RBR duo TD, 82445
HBK10	TD02	10 Dec 2018	9 Jun 2019	182	77.0029	15.6311	22	RBR duo TD, 82446
ISBW1	P06	26 May 2015	7 Jun 2015	13	77.0003	15.5628	9	RBR virtuoso P, 52916
ISBW2	Wave02	4 Jun 2015	3 Jun 2016	366	76.9974	15.5608	10	RBR virtuoso wave, 55112
ISBW3	Wave05	13 Jun 2016	23 May 2017	345	76.9977	15.5605	10	RBR virtuoso wave, 55112
ISBW4	Wave07	3 Jun 2017	22 May 2018	354	76.9977	15.5599	10	RBR virtuoso wave, 55112
ISBE1	Wave03	4 Jun 2015	3 Jun 2016	366	77.0044	15.5935	10	RBR virtuoso wave, 55112
RET1	P07	13 Jul 2015	25 Jul 2015	13	76.9943	15.5308	11	RBR virtuoso P, 52915
GAS1	P08	13 Jul 2015	25 Jul 2015	13	76.9418	15.8117	8	RBR virtuoso P, 52916
GAS2	P09	16 Aug 2015	9 Sep 2015	25	76.9416	15.8482	8	RBR virtuoso P, 52915
GAS3	Wave06	17 Jun 2016	2 Jun 2017	351	76.9540	15.8850	11	RBR virtuoso wave, 55113
GAS4	Wave10	5 Jun 2018	10 Jun 2019	371	76.9506	15.7710	22	RBR virtuoso wave, 55113
GAS5	Wave12	26 Jun 2019	14 Jan 2021	569	76.9505	15.7735	23	RBR virtuoso wave, 55113
VES1	P10	16 Aug 2015	13 Sep 2015	29	76.9957	15.4876	11	RBR virtuoso P, 52916
VES2	Wave09	5 Jun 2018	9 Jun 2019	370	76.9951	15.4881	16	RBR virtuoso wave, 55112
VES3	Wave11	25 Jun 2019	12 Feb 2021	599	76.9952	15.4894	16	RBR virtuoso wave, 55112

For consistency, the raw data were subsampled to 1024 s bursts at 60 min interval (starting at full hours) with 1 Hz sampling interval. The erroneous bursts at the start and end of deployments were removed. The datasets were cropped to full days so that the first measurement occurs at 00:00:00 UTC (hh:mm:ss) and the last one at 23:17:03 (1024 s after 23:00). These 24 deployment files are time series with three columns representing time, burst number and raw pressure (in dbar), and they are available as part of the dataset (Swirad et al., 2023).

3.2 Burst processing

The deployment files were imported into Spyder (Python 3.9) and processed on the burst-by-burst basis, with an algorithm described below (see also Wang et al., 1986; Karimpour and Chen, 2017; Marino et al., 2022, and references therein). Importantly, all steps described below are based on the linear wave theory; alternative data processing methods (e.g. Bonneton et al., 2018) might be applied to the original burst data to capture non-linear effects, but they are not considered here.

Hourly (one per burst) atmospheric pressure P_{air} (mbar) data at sea level were taken from the Polish Polar Station archive (<https://monitoring-hornsund.igf.edu.pl/>, last access:

28 March 2022). The water pressure, P_{sea} (dbar), was calculated by subtracting atmospheric pressure from the raw pressure, P_{raw} :

$$P_{\text{sea}} = P_{\text{raw}} - P_{\text{air}}/100. \quad (1)$$

Depth, z (m), was calculated using the UNESCO formula (Fofonoff and Millard, 1983) under assumption of constant water temperature of 0 °C, salinity of 35 PSU and latitude $\varphi = 77^\circ \text{N}$:

$$z = \left[\left(\left(\left(-1.82 \times 10^{-15} P_{\text{sea}} + 2.279 \times 10^{-10} \right) P_{\text{sea}} - 2.2512 \times 10^{-5} \right) P_{\text{sea}} + 9.72659 \right) P_{\text{sea}} \right] / g, \quad (2)$$

where g (ms^{-2}) denotes acceleration due to gravity, computed as

$$g = 9.780318[1 + (5.2788 \times 10^{-3} + 2.36 \times 10^{-5}x)] + 1.092 \times 10^{-6} P_{\text{sea}}, \quad (3)$$

and x is given by

$$x = \sin^2(\varphi/57.29578). \quad (4)$$

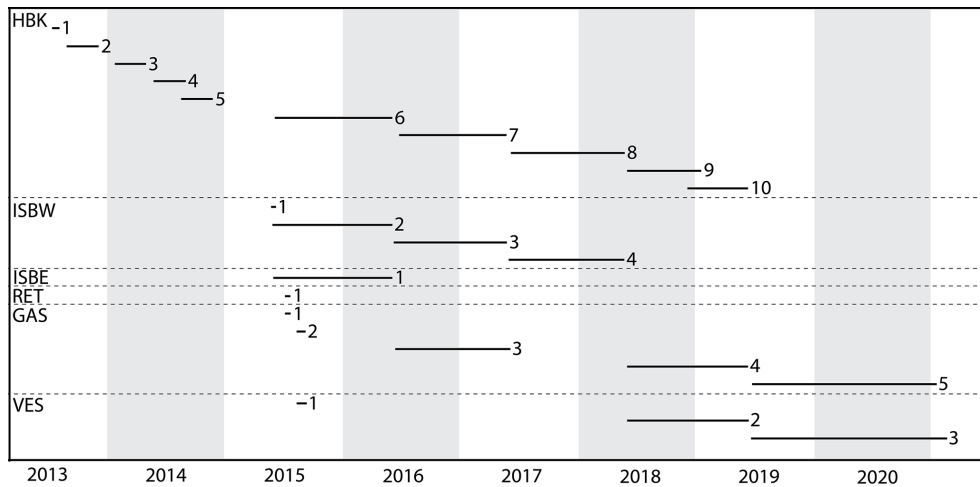


Figure 2. Time span of pressure sensor deployments for in situ wave measurements in Hornsund, Svalbard. HBK = Hansbukta, ISB = Isbjørnhamna (W = western, E = eastern), RET = Rettkvalbogen, GAS = Gåshamna, VES = Veslebogen.

The slowly varying component of water depth (due to, for example, tide and storm surge) was removed by subtracting from z a least-square-fitted second-order polynomial trend, z_{lf} , resulting in time series z_{hf} (m), related to depth variability associated with wind waves: $z_{hf} = z - z_{lf}$. The energy density spectrum at depth z , $E_z(f)$ (in $m^2 s$), was computed by applying fast Fourier transform (FFT; Frigo and Johnson, 2005) to the time series z_{hf} . As already mentioned, the data length used for FFT input was 1024. The Python `fft` function with default settings was used to compute the spectra, and no windowing was applied.

Finally, the spectrum at the sea surface, $E_0(f)$, was computed from $E_z(f)$ by applying a correction factor $A(f)$ accounting for the decrease of the wave orbital motion (and thus pressure fluctuations) with depth (compare red and blue spectra in Fig. 3):

$$E_0(f) = E_z(f)/A(f). \tag{5}$$

To this end, a set K of basic wavenumber values was defined, $K = \{0, 0.01, 0.02, \dots, 1000\} (m^{-1})$, and a corresponding set of basic wave frequencies, F , with the following elements:

$$f_i = \sqrt{gk_i \tanh(k_i h)} / (2\pi), \text{ for each } k_i \in K. \tag{6}$$

The set of correction factors A is then given by

$$A_i = \cosh(k_i (\bar{h} - \bar{z}_{lf})) / \cosh(k_i \bar{h}) \text{ for each } k_i \in K, \tag{7}$$

where \bar{h} and \bar{z}_{lf} denote the mean bottom depth and the mean logger depth, respectively (in the present case, with loggers mounted at the bottom, $\bar{h} = \bar{z}_{lf}$; averaging takes place over burst duration). The correction factor in Eq. (5) was calculated by linearly interpolating F and A to the frequencies of

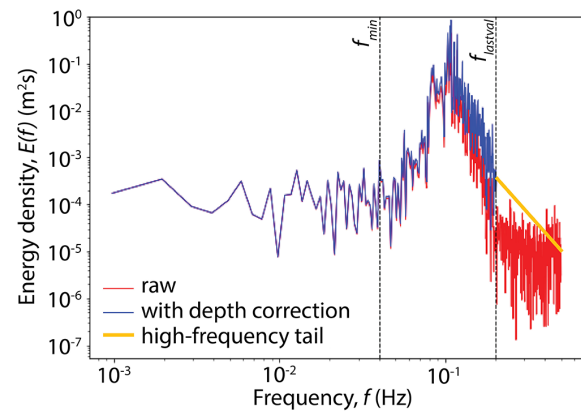


Figure 3. An example of wave energy density spectrum computed with the algorithm described in the text (deployment HBK9 burst no. 1): raw spectrum $E_z(f)$ at the depth of the logger (red), depth-corrected spectrum $E_0(f)$ (blue), and the analytical high-frequency tail (yellow). Frequency $f_{min} = 0.04$ Hz is the minimum frequency used to calculate mean wave parameters, and $f_{lastval}$ is the highest frequency reliably measured. The plot is limited to $f = 0.5$ Hz, which is the upper limit of the observation data. Wave parameters are calculated in two versions: for $f_{min} < f < f_{lastval}$ and for $f_{min} < f < \infty$.

the energy spectrum. (Note that g in expression 6 was computed from Eqs. 3 and 4 without the last term in Eq. 3, i.e. for $P_{sea} = 0$.)

As $A(f)$ quickly decreases with increasing wave frequency, the values of $E_0(f)$ computed from Eq. (5) become unreliable for f higher than some limiting frequency $f_{lastval}$. Here, $f_{lastval}$ was computed for each spectrum separately, based on a universal (constant for all spectra) limiting value of A : $A_{lim} = 0.05$ (note that, consistent with the linear wave theory used throughout this analysis, the values of A depend

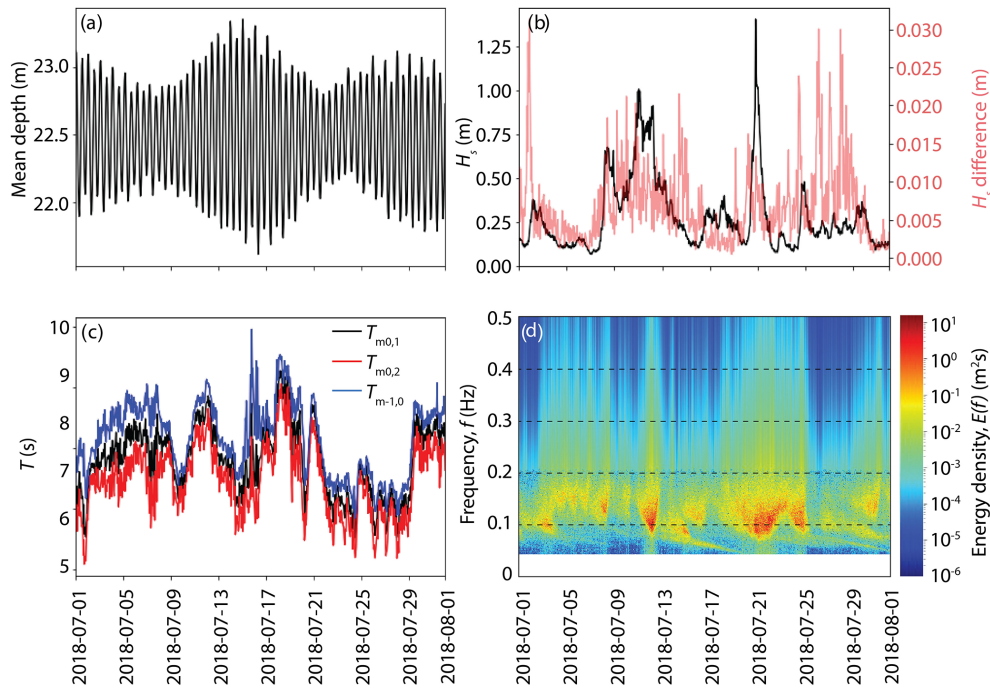


Figure 4. An example of outputs for 1 month (July 2018) of deployment HBK9: **(a)** mean depth \bar{z}_{lf} ; **(b)** primary y axis: significant wave height, H_s for $f_{\max} = \infty$, secondary y axis: the difference between H_s for $f_{\max} = \infty$ and for $f_{\max} = f_{\text{lastval}}$; **(c)** wave period, T , for $f_{\max} = \infty$; **(d)** wave energy spectra $E_0(f)$.

only on water depth and frequency of a given spectral component but not on the amplitude of that component). That is, f_{lastval} is the highest frequency for which $A > A_{\text{lim}}$. For all $f > f_{\text{lastval}}$, a high-frequency tail of the form $E_0(f) \sim f^{-4}$ was added after Kaihatu et al. (2007) by extrapolating the trend from the last $n = 10$ reliably estimated $E_0(f)$ values (yellow line in Fig. 3):

$$E_0(f) = \tilde{E}_0 f^{-4} \text{ for } f > f_{\text{lastval}}, \tag{8}$$

where

$$\tilde{E}_0 = \sum_{j=0}^{n-1} E_0(f_{\text{lastval}-j}) f_{\text{lastval}-j}^{-4} / \sum_{j=0}^{n-1} f_{\text{lastval}-j}^{-8}. \tag{9}$$

3.3 Mean wave parameters

In calculation of mean (integral) wave parameters, frequencies $f < f_{\min} = 0.04$ Hz (corresponding to wave periods higher than 25 s) were ignored. This limit corresponds to the approximate boundary between wind-generated and infragravity waves, as well as to the lower-frequency limit typically used in spectral wave models (e.g. Holthuijsen, 2007). Thus, the mean wave parameters were computed for $f_{\min} < f < f_{\max}$. In the final dataset, two sets of those parameters are provided, referred to as observational one (for $f_{\max} = f_{\text{lastval}}$) and modelled one (for $f_{\max} = \infty$). The spec-

tral moments m_n of $E_0(f)$ are defined as

$$m_n = \int_{f_{\min}}^{f_{\text{lastval}}} E_0(f) f^n df + C \frac{1}{3-n} \tilde{E}_0 f_{\text{lastval}}^{n-3} \text{ for } n \in N, \tag{10}$$

where \tilde{E}_0 is computed from Eq. (9), $C = 0$ if $f_{\max} = f_{\text{lastval}}$ and $C = 1$ if $f_{\max} = \infty$. Based on m_n , the following wave parameters are calculated: the significant wave height H_s , the mean absolute wave period $T_{m0,1}$, the mean absolute zero-crossing period $T_{m0,2}$, and the so-called energy period $T_{m-1,0}$:

$$H_s = 4\sqrt{m_0}, \tag{11}$$

$$T_{m0,1} = m_0/m_1, \tag{12}$$

$$T_{m0,2} = \sqrt{m_0/m_2}, \tag{13}$$

$$T_{m-1,0} = m_{-1}/m_0. \tag{14}$$

3.4 Output data

There are two output files for each deployment with rows representing bursts. The first one (“DepID_properties.txt”) contains the information on burst (number and time), mean water depth \bar{z}_{lf} , f_{lastval} , and the four mean wave parameters defined in Eqs. (11)–(14), in two versions, i.e. for $C = 0$ and $C = 1$,

Table 2. Dataset content. “DepID” stands for deployment ID.

File name	Number of files	Type	Rows	Columns
DepID.txt	24	input	Single measurements at 1 Hz frequency (full seconds) in 1024-element bursts (hh:00:00 to hh:17:03) starting at full hours UTC	1. Time [‘yyyy-mm-dd hh:mm:ss’] 2. Burst ID [1 : n] 3. Measured pressure (dbar)
airpressure.txt	1	input	Hourly measurements starting 21 July 2013 00:00:00 UTC	1. Atmospheric pressure at the sea level (mbar)
bursts2waves.py	1	code	n/a	n/a
DepID_properties.txt	24	output	Single bursts	1. Burst ID [1 : n] 2. Time [‘yyyy-mm-dd hh:mm:ss’] 3. Mean depth $\bar{z} _f$ (m) 4. f_{lastval} (Hz) 5. H_s (m) for $f_{\text{max}} = f_{\text{lastval}}$ 6. $T_{m0,1}$ (s) for $f_{\text{max}} = f_{\text{lastval}}$ 7. $T_{m0,2}$ (s) for $f_{\text{max}} = f_{\text{lastval}}$ 8. $T_{m-1,0}$ (s) for $f_{\text{max}} = f_{\text{lastval}}$ 9. H_s (m) for $f_{\text{max}} = \infty$ 10. $T_{m0,1}$ (s) for $f_{\text{max}} = \infty$ 11. $T_{m0,2}$ (s) for $f_{\text{max}} = \infty$ 12. $T_{m-1,0}$ (s) for $f_{\text{max}} = \infty$
DepID_spectra.txt	24	output	Single bursts	1–472. Wave energy density $E(f)$ ($\text{m}^2 \text{s}$) at 0.040039 to 0.5 Hz with a 1/1024 Hz step

n/a: not applicable.

respectively, in Eq. (10). The second file provides wave energy spectra for frequencies from 0.040039 to 0.5 Hz with step $\Delta f = \frac{1}{1024}$ Hz (472 columns). Figure 4 provides a visualisation of an example 1-month period of data. Table 2 provides the dataset content (Swirad et al., 2023).

3.5 Quality control

The instruments remained at the seabed thanks to the anchor weight. However, a few times they were transported by ice or strong waves resulting in an abrupt change in mean depth visible in the output data (e.g. Fig. 5a). This situation occurred three times: in VES1 bursts no. 83 (depth rise of ~ 1 m) and no. 370 (depth drop of ~ 2.3 m) and in GAS5 burst no. 13 420 (depth rise of ~ 0.7 m). In the case of VES1 burst no. 83 and GAS5 burst no. 13 420, it occurred in between bursts with no impact on calculated wave energy spectra and bulk parameters. Therefore, the data are left unchanged. If the dataset is used for tide analysis, time series should be split at the depth change event and treated separately. To identify erroneous bursts, we investigated the energy density for $f < 0.5$ Hz and identified two bursts with abnormally high energy density at low frequencies that resulted in erroneous calculation of bulk parameters (e.g. Fig. 5b): VES1 burst no. 370 and HBK1 burst no. 44. In the first case, the error resulted from instrument displacement during the burst. In the second case, mean

depth rose by ~ 0.5 m, remained higher for a few hours and dropped back to a typical level. There was no anomaly in atmospheric pressure and we speculate that the artefact may be due to the presence of glacier ice at the sea surface. In both cases, we replaced all output wave parameters with “NaN” (not a number).

4 Results

For all bays except Rettkvalbøgen, time series length exceeded 1 year, providing information on seasonal variability in wind wave conditions. The largest waves characterise Veslebøgen, the western-most of the analysed northern bays (Fig. 6). Mean full dataset H_s ranged from 0.25 m in eastern Isbjørnhamna to 0.43 m in Veslebøgen, and respective 99th percentile H_s values equalled 1.21 and 1.96 m. Waves were the highest in the first and last quarters of the year with the highest mean H_s of 0.53 m in October–December and 99th percentile H_s of 2.32 m in January–March, both in Veslebøgen (Table 3). A seasonal trend is also clearly visible in Fig. 7. Winter months are characterised by generally higher and longer waves, a finding consistent with the multi-decadal wave model reanalysis of Wojtysiak et al. (2018) for open Greenland Sea, west of Hornsund.

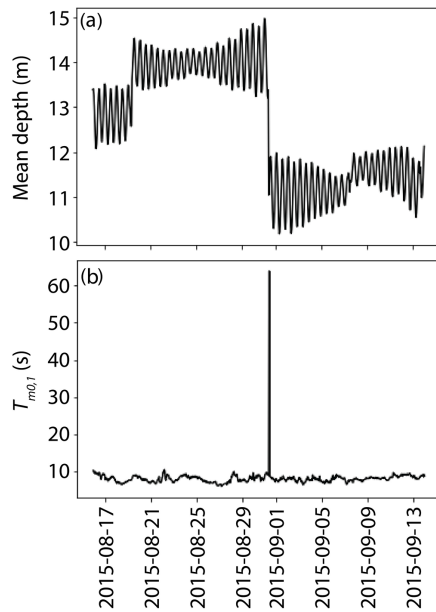


Figure 5. An example of data errors for deployment VES1: (a) mean depth \bar{z}_f ; (b) mean wave period $T_{m0,1}$ for $f < 0.5$ Hz.

Table 3. Summary of significant wave height (H_s : mean, 99th percentile for the full dataset and by quarters of the year) and mean full dataset wave period (mean absolute wave period $T_{m0,1}$, mean absolute zero-crossing period $T_{m0,2}$, and energy period $T_{m-1,0}$). HBK = Hansbukta, ISB = Isbjørnhamna (W = western, E = eastern), GAS = Gåshamna, VES = Veslebogen. Rettkvalbogen (RET) is excluded as the 13 d duration is not sufficient to derive seasonal statistics.

	HBK	ISBW	ISBE	GAS	VES
Mean H_s (m)	0.33	0.26	0.25	0.26	0.43
99th percentile H_s (m)	1.71	1.5	1.21	1.33	1.96
Jan–Mar mean H_s (m)	0.44	0.34	0.33	0.35	0.5
Jan–Mar 99th percentile H_s (m)	2.06	1.76	1.5	1.54	2.32
Apr–Jun mean H_s (m)	0.21	0.13	0.16	0.2	0.35
Apr–Jun 99th percentile H_s (m)	0.97	0.48	0.72	1.18	1.71
Jul–Sep mean H_s (m)	0.23	0.16	0.17	0.17	0.35
Jul–Sep 99th percentile H_s (m)	1.03	0.82	1	0.79	1.48
Oct–Dec mean H_s (m)	0.43	0.4	0.35	0.34	0.53
Oct–Dec 99th percentile H_s (m)	1.96	1.91	1.25	1.47	2.25
Mean $T_{m0,1}$ (s)	9.51	9.2	8.31	8.84	9.19
Mean $T_{m0,2}$ (s)	8.72	8.23	7.33	7.93	8.39
Mean $T_{m-1,0}$ (s)	10.36	10.34	9.5	9.93	10.09

5 Data availability

The inputs, outputs and the Python code described in this paper are available in the PANGAEA repository (<https://doi.org/10.1594/PANGAEA.954020>; Swirad et al., 2023). Raw data downloaded from the instruments are part of the IG PAS LONGHORN oceanographic monitoring, and they are available at the IG PAS Data Portal (https://doi.org/10.25171/InstGeoph_PAS_IGData_NBP_2022_005; Swirad et al., 2022). As the monitoring programme is on-going, fu-

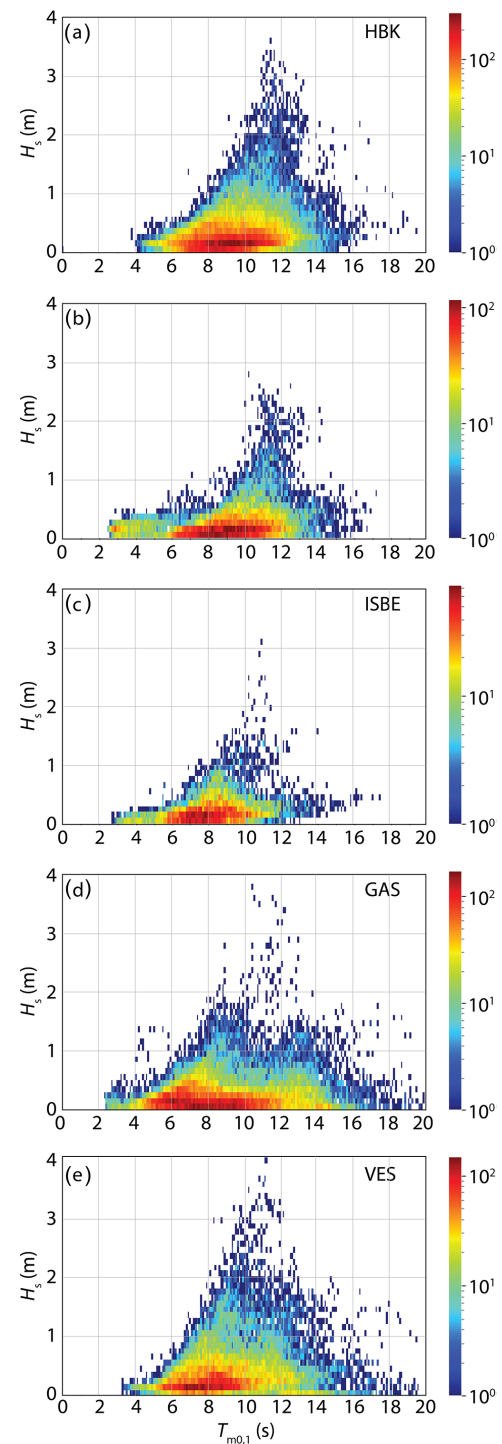


Figure 6. Distribution of significant wave height, H_s (y axis; range: 0–4 m with 0.1 m bins) and mean absolute wave period, $T_{m0,1}$ (x axis; range 0–20 s with 0.1 s bins) with $f_{\max} = \infty$ for (a) Hansbukta (HBK), (b) western Isbjørnhamna (ISBW), (c) eastern Isbjørnhamna (ISBE), (d) Gåshamna (GAS), and (e) Veslebogen (VES).

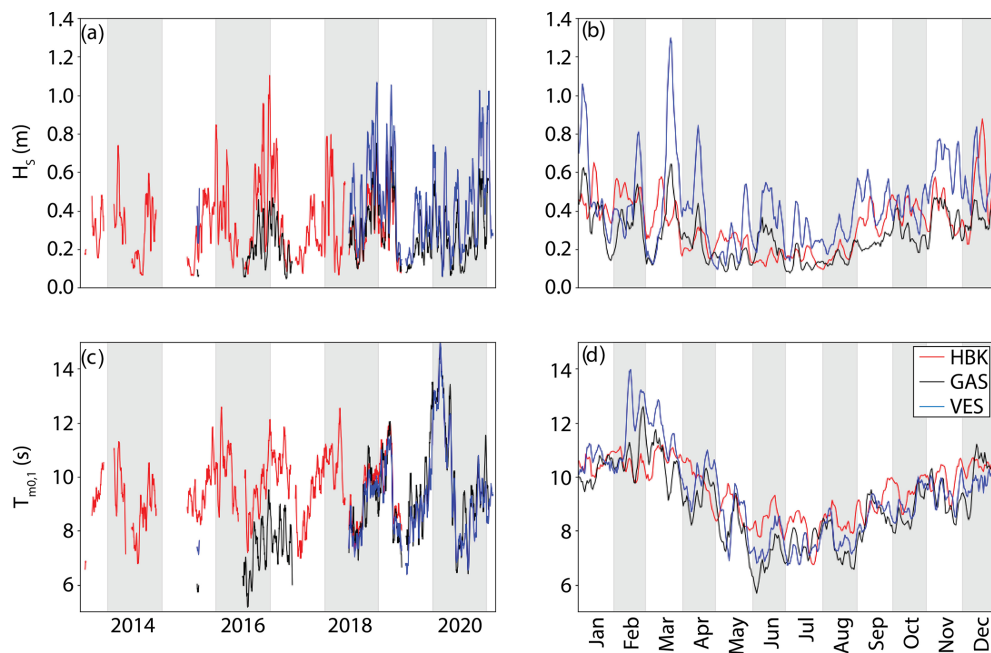


Figure 7. Summary of the wind wave characteristics for Hansbukta (HBK), Gåshamna (GAS) and Veslebogen (VES) for $f_{\max} = \infty$: (a) mean daily significant wave height, H_s , smoothed with a 15 d moving average; (b) mean daily significant wave height, H_s , for days of year smoothed with a 5 d moving average; (c) mean daily absolute wave period, $T_{m0,1}$, smoothed with a 15 d moving average; (d) mean daily absolute wave period, $T_{m0,1}$, for days of year smoothed with a 5 d moving average.

ture raw data and data processed in the same way as described here will be uploaded to the IG PAS Data Portal (<https://dataportal.igf.edu.pl/>, last access: 26 June 2023).

6 Summary

We present the first multi-year continuous wind wave and water level dataset for Hornsund fjord, Svalbard. Twenty four single deployments of underwater RBR sensors at 8–23 m depth between July 2013 and February 2021 were used to measure water levels in five bays of northern Hornsund (Hansbukta, western Isbjørnhamna, eastern Isbjørnhamna, Rettkvalbogen, Veslebogen) and one of southern (Gåshamna) Hornsund. Raw data (Swirad et al., 2022) were subsampled to 1024 s sets (\sim bursts) at 1 Hz measurement interval at 1 h burst interval, and they were then used to derive mean water levels, wave spectra and bulk wave parameters. We describe the procedure (available also as a Python code) that includes subtracting atmospheric pressure, depth calculation, fast Fourier transform, correction for the decrease of the wave orbital motion with depth and adding a high-frequency tail. We performed quality control on the output data. The dataset can be used to, for example, characterise wind wave climate in Hornsund; identify seasonal to inter-annual trends; calibrate and validate wave models (as shown by Herman et al., 2019); and facilitate analysis of sea-ice impact on wave attenuation, empirical modelling of wave run-up on Arctic beaches, and predicting future change. We pro-

vide individual bursts with pressure time series and the code for the users to apply different analysis methods, use alternative algorithm parameters, analyse non-linear effects, etc., depending on the application.

Author contributions. MM initiated and maintains the oceanographic monitoring in Hornsund. ZMS secured the funding. ZMS wrote the code and processed the data with support from AH and MM. All authors wrote the paper.

Competing interests. The contact author has declared that none of the authors has any competing interests.

Disclaimer. Publisher’s note: Copernicus Publications remains neutral with regard to jurisdictional claims in published maps and institutional affiliations.

Acknowledgements. We thank Kacper Wojtysiak for sharing his MATLAB code, Aleksandra Stępień and Adam Stucki (Hańcza-TECH) for helping in the underwater work, and the Polar Polish Station crew for maintaining the oceanographic and meteorological monitoring. We are grateful to Tsubasa Kodaira and an anonymous reviewer for constructive comments.

Financial support. This study was funded by the National Science Centre of Poland (grant no. 2021/40/C/ST10/00146). Acquisition of raw data (Swirad et al., 2022) was funded by the National Science Centre of Poland (grant no. 2013/09/B/ST10/04141) and IG PAS LONGHORN oceanographic monitoring in collaboration with Polish Polar Station Hornsund and the Ministry of Education and Science of Poland (statutory activities no. 3841/E-41/S/2022).

Review statement. This paper was edited by Giuseppe M.R. Manzella and reviewed by Tsubasa Kodaira and one anonymous referee.

References

- Ardhuin, F., Sutherland, P., Doble, M., and Wadhams, P.: Ocean waves across the Arctic: attenuation due to dissipation dominates over scattering for periods longer than 19 s: observed ocean wave attenuation across the arctic, *Geophys. Res. Lett.*, 43, 5775–5783, <https://doi.org/10.1002/2016GL068204>, 2016.
- Barnhart, K. R., Overeem, I., and Anderson, R. S.: The effect of changing sea ice on the physical vulnerability of Arctic coasts, *The Cryosphere*, 8, 1777–1799, <https://doi.org/10.5194/tc-8-1777-2014>, 2014.
- Błaszczczyk, M., Ignatiuk, D., Uszczyk, A., Cielecka-Nowak, K., Grabiec, M., Jania, J. A., Moskalik, M., and Walczowski, W.: Freshwater input to the Arctic fjord Hornsund (Svalbard), *Polar Res.*, 38, 3506, <https://doi.org/10.33265/polar.v38.3506>, 2019.
- Bonneton, P., Lannes, D., Martins, K., and Michallet, H.: A non-linear weakly dispersive method for recovering the elevation of irrotational surface waves from pressure measurements, *Coast. Eng.* 138, 1–8, <https://doi.org/10.1016/j.coastaleng.2018.04.005>, 2018.
- Booij, N., Ris, R. C., and Holthuijsen, L. H.: A third-generation wave model for coastal regions. 1. Model description and validation, *J. Geophys. Res.*, 104, 7649–7666, <https://doi.org/10.1029/98jc02622>, 1999.
- Carrasco, A., Saetra, Ø., Burud, A., Müller, M., and Melsom A.: Product user manual for Arctic Ocean Wave Analysis and Forecasting products ARCTIC_ANALYSIS_FORECAST_WAV_002_014, Issue: 1.6, Copernicus Marine Service, <https://doi.org/10.48670/moi-00002>, 2022.
- Dee, D. P., Uppala, S. M., Simmons, A. J., Berrisford, P., Poli, P., Kobayashi, S., Andrae, U., Balmaseda, M. A., Balsamo, G., Bauer, P., Bechtold, P., Beljaars, A. C. M., van de Berg, L., Bidlot, J., Bormann, N., Delsol, C., Dragani, R., Fuentes, M., Geer, A. J., Haimberger, L., Healy, S. B., Hersbach, H., Hólm, E. V., Isaksen, I., Kållberg, P., Köhler, M., Matricardi, M., McNally, A. P., Monge-Sanz, B. M., Morcrette, J.-J., Park, B.-K., Peubey, C., de Rosnay, P., Tavolato, C., Thépaut, J.-N., and Vitart, F.: The ERA-Interim reanalysis: configuration and performance of the data assimilation system, *Q. J. Roy. Meteor. Soc.*, 137, 553–597, <https://doi.org/10.1002/qj.828>, 2011.
- Fofonoff, N. P. and Millard Jr., R. C.: Algorithms for computation of fundamental properties of seawater, *UNESCO Technical Papers in Marine Science*, 44, <https://darchive.mblwhoilibrary.org/bitstream/handle/1912/2470/059832eb.pdf> (last access: 28 November 2022), 1983.
- Forbes, D.: State of the Arctic Coast 2010 – Scientific Review and Outlook, Tech. Rep., International Arctic Science Committee, Land-ocean Interactions in the Coastal Zone, Arctic Monitoring and Assessment Programme, International Permafrost Association, Helmholtz-Zentrum, Geesthacht, Germany, 178 pp., <http://arcticcoasts.org> (last access: 28 November 2022), 2011.
- Francis, O. P., Panteleev, G. G., and Atkinson, D. E.: Ocean wave conditions in the Chukchi Sea from satellite and in situ observations, *Geophys. Res. Lett.*, 38, L24610, <https://doi.org/10.1029/2011GL049839>, 2011.
- Frijo, M. and Johnson, S. G.: The Design and Implementation of FFTW3, *P. IEEE*, 93, 216–231, <https://doi.org/10.1109/JPROC.2004.840301>, 2005.
- Herman, A., Wojtysiak, K., and Moskalik, M.: Wind wave variability in Hornsund fjord, west Spitsbergen, *Estuar. Coast. Shelf S.*, 217, 96–109, <https://doi.org/10.1016/j.ecss.2018.11.001>, 2019.
- Hersbach, H., Bell, B., Berrisford, P., Hirahara, S., Horányi, A., Muñoz-Sabater, J., Nicolas, J., Peubey, C., Radu, R., Schepers, D., Simmons, A., Soci, C., Abdalla, S., Abellan, X., Balsamo, G., Bechtold, P., Biavati, G., Bidlot, J., Bonavita, M., De Chiara, G., Dahlgren, P., Dee, D., Diamantakis, M., Dragani, R., Flemming, J., Forbes, R., Fuentes, M., Geer, A., Haimberger, L., Healy, S., Hogan, R. J., Hólm, E., Janisková, M., Keeley, S., Laloyaux, P., Lopez, P., Lupu, C., Radnoti, G., de Rosnay, P., Rozum, I., Vamborg, F., Villaume, S., and Thépaut, J. N.: The ERA5 global reanalysis, *Q. J. Roy. Meteor. Soc.*, 1–51, <https://doi.org/10.1002/qj.3803>, 2020.
- Holthuijsen, L.: *Waves in Oceanic and Coastal Waters*, Cambridge University Press, <https://doi.org/10.1017/CBO9780511618536>, 387 pp., 2007.
- IPCC: *The Ocean and Cryosphere in a Changing Climate*, International Panel on Climate Change, <https://www.ipcc.ch/srocc/home> (last access: 28 November 2022), 2019.
- Jakacki, J., Przyborska, A., Kosecki, S., Sundfjord, A., and Albretsen, J.: Modelling of the Svalbard fjord Hornsund, *Oceanologia*, 59, 473–495, <https://doi.org/10.1016/j.oceano.2017.04.004>, 2017.
- Kaihatu, J., Veeramony, J., Edwards, K., and Kirby, J.: Asymptotic behaviour of frequency and wave number spectra of nearshore shoaling and breaking waves, *J. Geophys. Res.*, 112, C06016, <https://doi.org/10.1029/2006JC003817>, 2007.
- Karimpour, A. and Chen, Q.: Wind wave analysis in depth limited water using OCEANLYZ, A MATLAB toolbox, *Comput. Geosci.* 106, 181–189, <https://doi.org/10.1016/j.cageo.2017.06.010>, 2017.
- Kowalik, Z., Marchenko, A., Brazhnikov, D., and Marchenko, N.: Tidal currents in the western svalbard fjords, *Oceanologia*, 57, 318–327, <https://doi.org/10.1016/j.oceano.2015.06.003>, 2015.
- Marino, M., Rabionet, I. C., and Musumeci, R. E.: Measuring free surface elevation of shoaling waves with pressure transducers, *Cont. Shelf Res.*, 245, 104803, <https://doi.org/10.1016/j.csr.2022.104803>, 2022.
- Muckenhuber, S., Nilsen, F., Korosov, A., and Sandven, S.: Sea ice cover in Isfjorden and Hornsund, Svalbard (2000–2014) from remote sensing data, *The Cryosphere*, 10, 149–158, <https://doi.org/10.5194/tc-10-149-2016>, 2016.

- Nederhoff, K., Erikson, L., Engelstad, A., Bieniek, P., and Kasper, J.: The effect of changing sea ice on wave climate trends along Alaska's central Beaufort Sea coast, *The Cryosphere*, 16, 1609–1629, <https://doi.org/10.5194/tc-16-1609-2022>, 2022.
- Reistad, M., Breivik, Ø., Haakenstad, H., Aarnes, O. J., Furevik, B. R., and Bidlot, J.-R.: A high-resolution hindcast of wind and waves for the North Sea, the Norwegian Sea, and the Barents Sea. *J. Geophys. Res.*, 116, C05019, <https://doi.org/10.1029/2010JC006402>, 2011.
- Saha, S., Moorthi, S., Wu, X., Wang, J., Nadiga, S., Tripp, P., Behringer, D., Hou, Y.-T., Chuang, H.-Y., Iredell, M., Ek, M., Meng, J., Yang, R., Mendez, M. P., van den Dool, H., Zhang, Q., Wang, W., Chen, M., and Becker, E.: The NCEP Climate Forecast System Version 2, *J. Climate*, 27, 2185–2208, <https://doi.org/10.1175/jcli-d-12-00823.1>, 2014.
- Semedo, A., Vettor, R., Breivik, Ø., Sterl, A., Reistad, M., Guedes Soares, C., and Lima, D.: The wind sea and swell waves climate in the Nordic seas, *Ocean Dynam.*, 65, 223–240, <https://doi.org/10.1007/s10236-014-0788-4>, 2015.
- Stopa, J. E., Arduin, F., and Girard-Arduin, F.: Wave climate in the Arctic 1992–2014: seasonality and trends, *The Cryosphere*, 10, 1605–1629, <https://doi.org/10.5194/tc-10-1605-2016>, 2016.
- Swirad, Z. M., Moskalik, M., and Glowacki, O.: Sea pressure and wave monitoring datasets in Hornsund fjord, IG PAS Data Portal [data set], https://doi.org/10.25171/InstGeoph_PAS_IGData_NBP_2022_005, 2022.
- Swirad, Z. M., Moskalik, M., and Herman, A.: In situ wind wave and water level measurements in Hornsund, Svalbard in 2013–2021, PANGAEA [data set], <https://doi.org/10.1594/PANGAEA.954020>, 2023.
- Uppala, S. M., Kållberg, P. W., Simmons, A. J., Andrae, U., Da Costa Bechtold, V., Fiorino, M., J. K. Gibson, J. K., Haseler, J., Hernandez, A., Kelly, G. A., Li, X., Onogi, K., Saarinen, S., Sokka, N., Allan, R. P., Andersson, E., Arpe, K., Balmaseda, M. A., Beljaars, A. C. M., Van De Berg, L., Bidlot, J., Bormann, N., Caires, S., Chevallier, F., Dethof, A., Dragosavac, M. Fisher, M. Fuentes, M., Hagemann, S., Hólm, E., Hoskins, B. J., Isaksen, L., Janssen, P. A. E. M., Jenne, R., McNally, A. P., Mahfouf, J.-F., Morcrette, J.-J., Rayner, N. A., Saunders, R. W. Simon, P., Sterl, A., Trenberth, K. E., Untch, A. Vasiljevic, D., Viterbo, P., and Woollen J.: The ERA40 reanalysis, *Q. J. Roy. Meteor. Soc.*, 131, 2961–3012, <https://doi.org/10.1256/qj.04.176>, 2005.
- Wang, H., Lee, D.-Y., and Garcia, A.: Time series surface-wave recovery from pressure gage, *Coast. Eng.*, 10, 379–393, [https://doi.org/10.1016/0378-3839\(86\)90022-0](https://doi.org/10.1016/0378-3839(86)90022-0), 1986.
- Wang, X. L., Feng, Y., Swail, V. R., and Cox, A.: Historical changes in the Beaufort–Chukchi–Bering seas surface winds and waves, 1971–2013, *J. Climate*, 28, 7457–7469, <https://doi.org/10.1175/JCLI-D-15-0190.1>, 2015.
- Waseda, T., Webb, A., Sato, K., Inoue, J., Kohout, A., Penrose, B., and Penrose, S.: Correlated increase of high ocean waves and winds in the ice-free waters of the Arctic Ocean, *Sci. Rep.*, 8, 4489, <https://doi.org/10.1038/s41598-018-22500-9>, 2018.
- Wawrzyniak, T. and Osuch, M.: A 40-year High Arctic climatological dataset of the Polish Polar Station Hornsund (SW Spitsbergen, Svalbard), *Earth Syst. Sci. Data*, 12, 805–815, <https://doi.org/10.5194/essd-12-805-2020>, 2020.
- Wojtysiak, K., Herman, A., and Moskalik, M.: Wind wave climate of west Spitsbergen: seasonal variability and extreme events, *Oceanologia*, 60, 331–343, <https://doi.org/10.1016/j.oceano.2018.01.002>, 2018.
- WW3DG: User manual and system documentation of WAVEWATCH III R version 6.07, Tech. Note 333, The WAVEWATCH III R Development Group, NOAA/NWS/NCEP/MMAB, College Park, MD, USA, 465 pp. + Appendices, <https://github.com/NOAA-EMC/WW3/wiki/files/manual.pdf> (last access: 28 November 2022), 2019.
- Zagórski, P., Rodzik, J., Moskalik, M., Strzelecki, M. C., Lim, M., Błaszczuk, M., Promińska, A., Kruszewski, G., Styszyńska, A., and Malczewski, A.: Multidecadal (1960–2011) shoreline changes in Isbjørnhamna (Hornsund, Svalbard), *Pol. Polar Res.*, 36, 369–390, 2015.
- Zhao, X., Shen, H. H., and Cheng, S.: Modeling ocean wave propagation under sea ice covers, *Acta Mech. Sinica Xuebao*, 31, 1–15, <https://doi.org/10.1007/s10409-015-0017-5>, 2015.